The study of Cu/Fe-doped Al-MCM-41 to degrade Rhodamine B

Shunyi Li, Shaohua Wang, Qiang Chen, Suyu Jiang and Shaohui Sun

ABSTRACT

Textile wastewater has been recognized as one of the most difficult to treat environmental problems. Aiming to acquire an excellent treatment effect that could meet the stringent discharge regulations, a series of Cu- and Fe-doped Al-MCM-41 heterogeneous Fenton catalysts with different metal contents (1.21–3.45 wt%) were successfully synthesized by co-precipitation method to degrade Rhodamine B. Their physicochemical properties were analysed by X-ray diffraction, X-ray photoelectron spectroscopy, Fourier transform infrared spectroscopy, nitrogen physisorption and scanning electron microscopy. The incorporation of metal did not alter MCM-41's mesostructure, but increasing the contents of metal would decrease the order of MCM-41s' structure. The effects of temperature, pH, H_2O_2 dosage, dye concentration and the dosage of catalysts on Rhodamine B degradation were also investigated. It was found that M2 with 2.71 wt% of active metals performed best on Rhodamine B degradation. For the high concentration of Rhodamine B (400 mg/L), the decolorization efficiency could reach 96.0% using only 40 mM H_2O_2 within 50 min at 60 °C. Further adding 40 mM of H_2O_2, the chemical oxygen demand removal reached 75.1% after 100 min. M2 showed excellent stability and could be reused at least three times without any obvious deterioration in catalytic activity. M2 fitted well with the Freundlich isotherms and the first-order rate model.

Key words | catalytic degradation, copper oxide, doping, H_2O_2, iron oxide, MCM-41

HIGHLIGHTS

- A series of Cu- and Fe-doped Al-MCM-41 heterogeneous catalysts were synthesized to degrade RhB.
- The structure of MCM-41 was preserved.
- Catalysts had efficient and stable treatment performance.
- The adsorption model and the reaction kinetic model were further studied.
- The conditions of the RhB degradation reaction were optimized.

Shunyi Li
Shaohua Wang
School of Ecology and Environment,
Zhengzhou University,
Zhengzhou,
China

Qiang Chen
Suyu Jiang (corresponding author)
Shaohui Sun
School of Chemical Engineering,
Zhengzhou University,
Zhengzhou,
China
E-mail: *suyujiang@zzu.edu.cn*

Suyu Jiang
Shaohui Sun
Engineering Research Center of Advanced Functional Material Manufacturing of Ministry of Education, School of Chemical Engineering,
Zhengzhou University,
Zhengzhou 450001,
China

doi: 10.2166/wst.2021.090

GRAPHICAL ABSTRACT

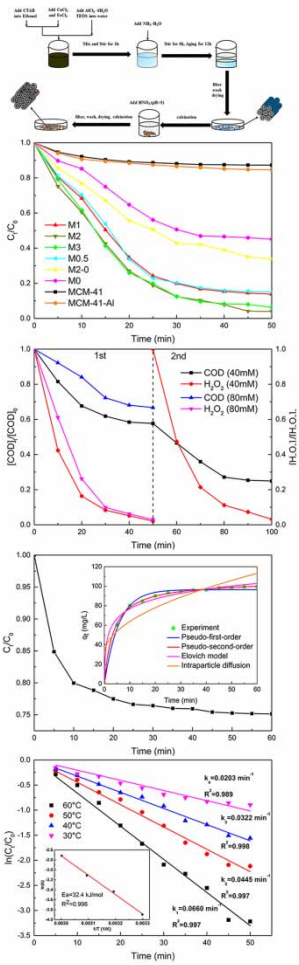

INTRODUCTION

With the rapid development of economies, many countries have been confronted with serious challenges in environment treatment, especially in wastewater treatment. As one of the biggest water-consuming industries, the textile industry has been struggling with huge difficulties in environment protection due to the large volume of organic wastewater containing dyes, surface-active materials and textile auxiliaries (El-Sharkaway *et al.* 2020).

In recent years, under increasingly stringent industrial wastewater discharge standards, it has become difficult for traditional wastewater treatment processes such as adsorption, membrane separation and biological treatment to meet the new standards. By contrast, advanced oxidation processes have been widely applied in wastewater treatment for their extraordinary effect, especially in the area of treating recalcitrant organic contaminants with high chemical stability and low biodegradability, which is a suitable approach for the textile industry wastewater treatment (Bokare & Choi 2014).

Among various advanced oxidation processes, Fenton reaction has received widespread attention due to its low operating cost, less reagent waste, low toxicity, high efficiency and strong versatility. The classical Fenton reaction using homogeneous Fe^{2+}/Fe^{3+} as catalyst and H_2O_2 as reagents (Lu *et al.* 1999), as shown in Equation (1), is highly efficient due to the high oxidizing ability and non-selectivity of hydroxyl radical. However, to prevent ferrous and ferric ion hydrolysing and to maintain the reaction

rates, a strong acid condition (pH < 3) is required for the reaction. Furthermore, it is difficult to recycle soluble iron salts from treated water and the notorious iron oxide sludge needs further treatment. The most important drawback is the slow reduction from Fe^{3+} to Fe^{2+}, leading to consumption of large quantities of Fe^{2+} (Ma *et al.* 2018). Those drawbacks limit its applicability.

$$Fe^{2+} + H_2O_2 \rightarrow Fe^{3+} + OH\cdot + OH^- \quad (1)$$

In recent years, to overcome the above drawbacks, researchers have been paying more attention to heterogeneous Fenton or Fenton-like catalysts. Similar to iron, copper can also convert H_2O_2 into reactive oxidants via the catalytic redox cycle of Cu(II)/Cu(I) as shown in Equations (2)–(5) (Eberhardt *et al.* 1989). Also, the copper-based catalysts exhibited excellent catalytic activity even in neutral pH condition, which suggests a bright prospect in the industry application. Some researchers found that incorporating two metals together could acquire an efficient bimetallic catalyst by comparison with the monometallic catalyst (Eberhardt *et al.* 1989). Among them, the combination of copper and iron is the optimal candidate (Roonasi & Nezhad 2016). What is more, the synergistic effects of dual-metal redox couples would accelerate the slow reduction from Fe^{3+} to Fe^{2+} which is the rate-determining step of Fenton reaction (Dai *et al.* 2018).

$$Cu^{2+} + H_2O_2 \rightarrow Cu^{+} + HO_2\cdot + H^+ \quad (2)$$

$$2HO_2\cdot \rightarrow 2O_2^-\cdot + 2H^+ \rightarrow H_2O_2 + O_2 \quad (3)$$

$$Cu^{2+} + O_2^-\cdot \rightarrow Cu^{+} + O_2 \quad (4)$$

$$Cu^{+} + H_2O_2 \rightarrow Cu^{2+} + OH^- + OH\cdot \quad (5)$$

It is well-known that copper is a toxic heavy metal, so the application of a copper homogeneous Fenton system is often limited. To overcome this drawback, copper has been suggested to be immobilized on a porous solid substrate. Zeolites, mesoporous materials, pillared interlayered clays, polymeric resins and activated carbons have been used as supporting materials for heterogeneous Fenton-like reaction. Among them, the mesoporous materials family exhibited an excellent efficiency, especially MCM-41, attributed to its high surface area, larger pore volume, narrow pore diameter and high thermal stability (Alonso Lemus *et al.* 2010). After introducing some specific transition metal cations or metal complexes into MCM-41's structure, such as Fe, Co, Ni, Cu and Mn, the catalytic properties could be remarkably improved, as MCM-41 contains a large number of silanol groups at the surface, which could be bonded or anchored with these metal atoms and metal ions. Moreover, the large surface area would enhance adsorbability and provide more reaction activity sites (Corrêa *et al.* 1997). Introducing excessive metal into the framework of MCM-41 may destroy its structure and decrease its catalytic activity. It had been proved that aluminium could maintain the structure of MCM-41. So it is beneficial to introduce some aluminium into MCM-41 framework (Ling *et al.* 2014).

In this paper, we synthesized a series of Cu/Fe-doped Al-MCM-41 catalyst with different contents of Fe and Cu by a co-precipitation method. Comparing to aluminium-free or copper-free catalyst, all bimetal-doped Al-MCM-41 performed better dye degradation. We also studied the optimal Cu/Fe ratio and the effect of reaction parameters. The physicochemical properties, adsorption model and reaction kinetics are also discussed.

MATERIAL AND METHODS

Materials

Aluminium chloride hexahydrate ($AlCl_3{\cdot}6H_2O$), iron chloride anhydrous ($FeCl_3$), ethyl silicate (TEOS), hydrogen peroxide (H_2O_2 30 wt%), methylene blue (MB) and ammonia (25 wt%) were purchased from Sinopharm Chemical Reagent Co., Ltd. Hexadecyl trimethyl ammonium bromide (CTAB), Congo red (CR), methyl orange (MO), rhodamine B (RhB), iso-propanol (IPA) and benzoquinone (BQ) were purchased from Shanghai Macklin Biochemical Co., Ltd. Cupric chloride anhydrous ($CuCl_2$) was purchased from Adamas Reagent Co., Ltd. All chemicals were analytical grade without further purification.

Synthesis of catalysts

We used a typical co-precipitation method to synthesize catalysts and the detailed method is presented in Supporting Information. By changing the additive amounts of $CuCl_2$, $FeCl_3$ and $AlCl_3{\cdot}6H_2O$, we obtained a series of MCM-41 catalysts containing different amounts of metal. The designated names of different catalysts are shown in Table 1 and their actual metal contents were measured by inductively coupled plasma optical emission spectrometry (ICP-OES), shown in Table S1 (Supplementary Material). The flowchart of the method to synthesize the catalysts is summarized in Figure 1.

Table 1 | The relationship between the designated names of different catalysts and their metal contents

	Additive amounts of different metals			
Designated name	**$CuCl_2$ (g)**	**$FeCl_3$ (g)**	**$AlCl_3{\cdot}6H_2O$ (g)**	**Molar ratio**
MCM-41	0	0	0	–
M1	0.1424	0.1736	0.5168	1:1:1
M2	0.2848	0.1736	0.5168	2:1:1
M3	0.4272	0.1736	0.5168	3:1:1
M0.5	0.1424	0.3472	0.5168	1:2:1
M0	0	0.1736	0.5168	0:1:1
M2-0	0.2848	0.1736	0	2:1:0
MCM-41-Al	0	0	0.5168	0:0:1

Characterization of the samples

A powder X-ray diffraction (XRD) instrument (D8ADVANCE) was employed to determine the crystalline phases of mesoporous samples, at the range of 5–80° with the scanning speed of 0.5° per minute. The morphology of the catalyst was observed with a scanning electron microscope (SEM, Thermo Scientific/Helios G4 CX). The BET (Brunauer–Emmett–Teller) surface areas and pore size distribution of the samples were measured by an ASAP2460 gas adsorption analyser using nitrogen as the adsorption gas after pre-treatment at 423 K for 8 h. The results of surface functional groups were obtained by Fourier transform infrared spectroscopy (FT-IR, STA8000-Frontier/PerkinElmer) using KBr pellets of the solid samples and its scanning range was 400–4,000 cm^{-1}. The results of the surface metal valence state were obtained by an X-ray photoelectron spectrometer (XPS, AXIS Supra). The contents of copper ions and ferric ions of the samples were measured using ICP-OES (Shimadzu Multitype ICPE-9820).

Catalytic performance

RhB was used as the model compound to assess the activity of as-prepared catalysts. A certain amount of RhB was dissolved in 200 mL deionized water in a flask (250 mL) and a certain dosage of catalysts was added into the solution. The covered flask was put in a thermostatic oscillatory water bath to keep the system at a constant temperature. The pH of the suspension was adjusted by appropriate amounts of NaOH or HCl to a given value. The suspension containing catalysts and RhB was shaken for 25 min to achieve adsorption equilibrium. After being adsorbed for 25 min, the concentration of RhB was measured and taken as the initial concentration (C_0). Then, certain amounts of H_2O_2 (30 wt%) were added into the suspension to activate the reaction. We took 2 mL solution from the flask after a fixed time interval. The supernatant solution was collected by filtration for absorbency measurements of RhB using a UV-vis spectrophotometer (Shimadzu, UV-2600) and chemical oxygen demand (COD) measurements using a COD analyser (Hach, DR-1010). Aiming to test the stability of the catalyst, the used catalysts were collected by filtration and regenerated by washing, drying and calcining at 500 °C. The concentrations of leached metal ions in solution after reaction were measured by atomic absorption spectroscopy (AAS, ZEEnit700P). The concentration of

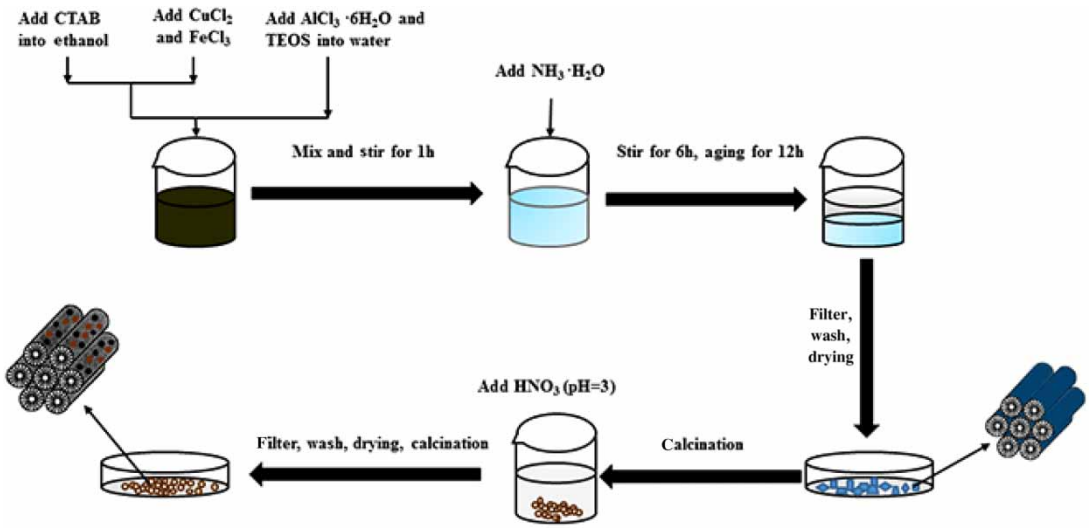

Figure 1 | Schematic representation of the method used to prepare the catalysts.

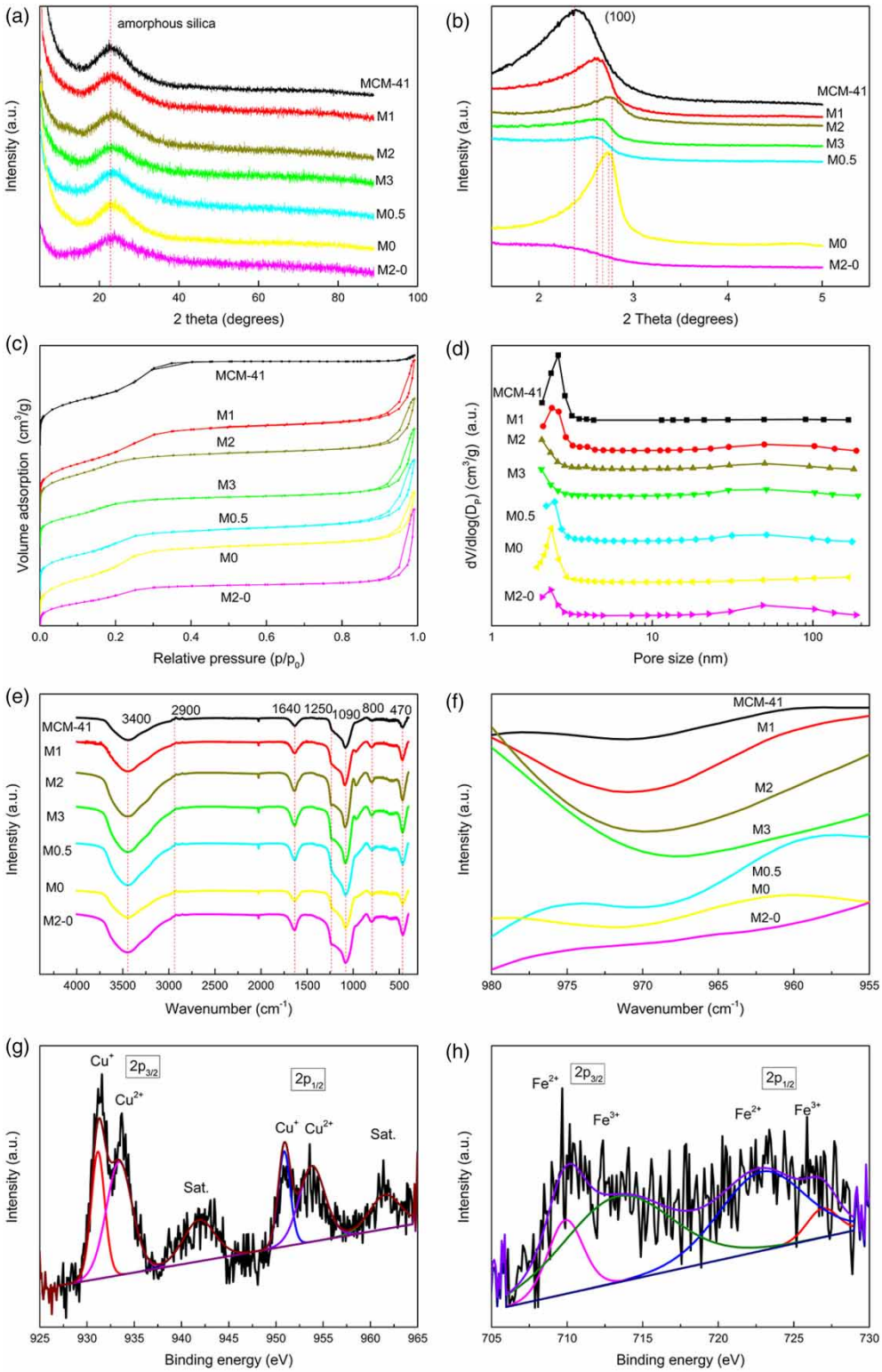

Figure 2 | XRD patterns, nitrogen adsorption isotherms, BJH pore size distributions, FT-IR spectra and XPS spectra of the samples. (a) The large-angle XRD patterns. (b) The small-angle XRD patterns. (c) Nitrogen adsorption isotherms of the samples. (d) BJH pore size distributions of the samples. (e) FT-IR spectra of the samples. (f) Partial FT-IR figure of the samples. (g) XPS spectra of Cu 2p; (h) XPS spectra of Fe 2p.

remaining H_2O_2 in the solution was measured according to Nogueira's method (Nogueira *et al.* 2005).

RESULTS AND DISCUSSION

Physicochemical characterizations

To analyse the crystal phase and mesoporous structure of samples, XRD analysis was performed, and results are shown in Figure 2(a) and 2(b). In the large-angle range (Figure 2(a)), it can be observed that all samples had a broad peak at about 23° which refers to amorphous silica (Xia *et al.* 2011a). Also, no other peak can be found in the large-angle range XRD patterns suggesting that metals were highly dispersed on the surface. In the small-angle range (Figure 2(b)), the XRD pattern of MCM-41 exposed a typical mesoporous structure with an intense reflection (100) and two weak reflections (110) and (200). With the incorporation of metal species, the (100) peak of other samples were preserved suggesting that MCM-41's mesoporous structures were retained. However, with the increase in the amounts of metal incorporation, the (100) peak intensities decreased gradually. M3 and M2 had a weak and broad (100) peak. This phenomenon indicated that the metal connected to the mesoporous framework and decreased the long-range hexagonal order (Parida & Rath 2007, 2009). Comparing with M2, M2-0 which possessed the same amounts of copper and iron but lacked Al did not preserve the (100) peak. This can be attributed to the fact that Al could sustain the structure of MCM-41 (Sobczak *et al.* 2004).

The nitrogen adsorption–desorption isotherms and BJH (Barrett–Joyner–Halenda) pore size distributions are shown in Figure 2(c) and 2(d). BET surface area, pore size, unit cell parameter (a_0) and pore volume of the samples are presented in Table S2.

All the samples exhibited the type IV N_2 adsorption isotherms according to the IUPAC classification, corresponding to the typical mesoporous MCM-41. All the curves sharpen at the relative pressure ($p/p_0 = 0.15$–0.35), which was typical of a capillary condensation process (Lin *et al.* 2000). Also, with the increasing amounts of metal incorporation, the curves turned to be more gentle, indicating partial loss of long-range order of the porous structure. It was consistent with the XRD results (Xia *et al.* 2011b). MCM-41 exhibited the Type H4 hysteresis loops which were associated with narrow slit-like pores (Sing *et al.* 1985) due to the existence of the void defects in the framework of MCM-41(Lin *et al.* 2000). Also, other samples showed a sharp and small hysteresis loop at the higher relative pressure ($p/p_0 > 0.8$), which may reflect the macropores of the interparticle (Sing *et al.* 1985; Kumar *et al.* 1994). As a result, the BJH average pore size of MCM-41 was the smallest among all samples and the BJH average pore size increased with the increase in the amounts of metal incorporation. Figure 3 vividly exhibits the variation trend of BET surface area and pore size with different metal contents. As can be seen from Table S2 and Figure 3, the BET surface area decreased with the increase of metal incorporation. Moreover, M2 and M3 had higher contents of metal than M2-0, but M2 and M3 possessed larger BET surface area. This phenomenon demonstrated that Al could sustain the structure of MCM-41.

The morphology of MCM-41, M1, M2 and M3 was characterized by SEM. The SEM images are shown in Figure 4 and Figure S1 (Supplementary Material). MCM-41 showed a typical image of silica microspheres with a narrow range of size distribution. Its average diameter was 250 ± 20 nm. The surface of silica microspheres was rough, suggesting that microspheres were composed of small spheres. As for M1 (shown in Figure S1(a) and S1(b)), silica microspheres became irregular and some silica microspheres broke into small spheres. Moreover, the broken small spheres tended to agglomerate together, resulting in the decrease in the surface area. With further increase in the amounts of incorporated metal, almost all silica microspheres of M2 and M3 (shown in Figure S1(c) and S1(d)) were broken into small spheres which agglomerated even more heavily. This was because the high contents of metal made unfavourable effects on the ordered MCM-41's structure, resulting in the agglomeration of samples.

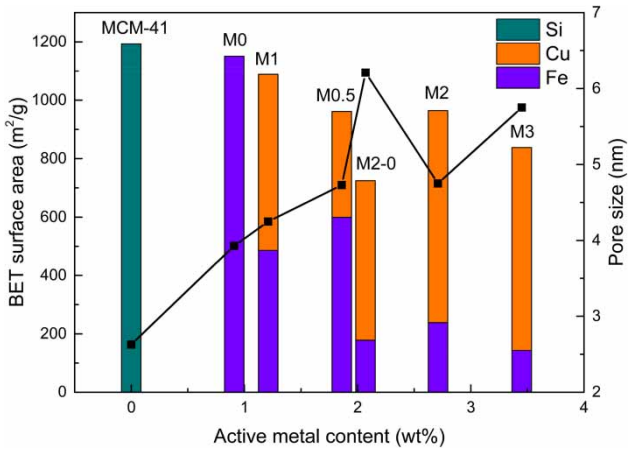

Figure 3 | The variation trend of BET surface area and pore size with the different contents of metal.

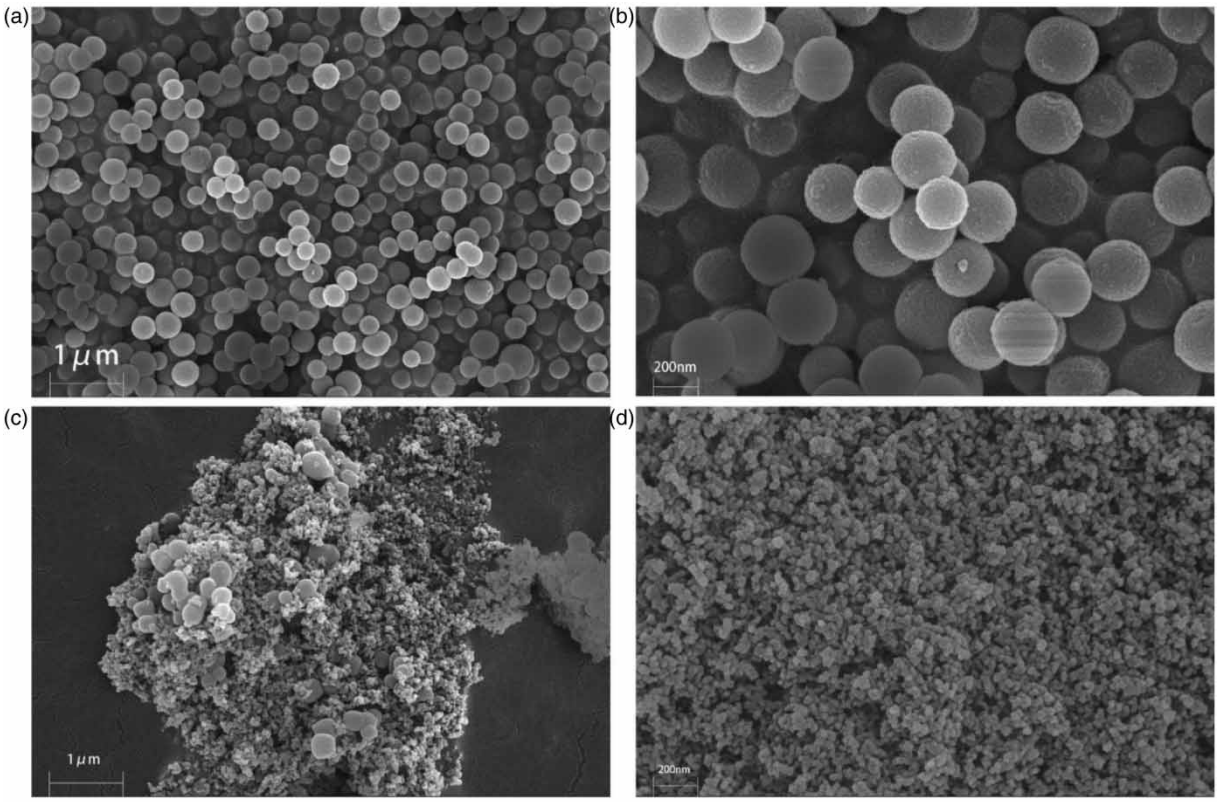

Figure 4 | SEM images of MCM-41 (a) and (b) and M2 (c) and (d).

This phenomenon was consistent with the results of the BET surface area.

The FT-IR adsorption spectra of samples are shown in Figure 2(e). The characteristic band at around 1,090 cm^{-1}, with a shoulder at 1,250 cm^{-1} (Kong *et al.* 2004), the band at around 800 cm^{-1} and the band at 470 cm^{-1} observed in all samples corresponded to the internal and external asymmetric Si-O stretching vibrations, the symmetric Si-O stretching and the deformation modes of SiO_4 tetrahedra in the Si-O-Si structure (tetrahedral bending of Si-O bonds), respectively (Liu *et al.* 2007). The strong adsorption band centred at around 1,640 cm^{-1} was assigned to the bending vibration of -OH; the broad band between 3,600 and 2,900 cm^{-1} was assigned to the surface hydroxyl group molecules (Parida & Rath 2009). The intensity of the above two bands increased with the increase of incorporated metals suggesting that greater amounts of metal would increase catalysts' hydrophilicity. This was because more contents of metal would increase the number of surface acid sites (Ling *et al.* 2014). The characteristic band at around 1,090 cm^{-1} was so intense that the band at around 970 cm^{-1} of some samples was difficult to be observed. So we made a partial FT-IR figure from 955 to 980 cm^{-1} as shown in Figure 2(f). MCM-41 exhibited a weak band at around 972 cm^{-1} which could be attributed to Si-O vibration in Si-OH group of siliceous MCM-41. When introducing metals into MCM-4's structure, the bands shift to lower wavenumber. This was due to the interaction between metal atoms (copper or iron) and silicon (forming M-O-Si bands) (Srinivas *et al.* 2002; Kong *et al.* 2004). The length of Cu-O band and Fe-O are greater than the length of Si-O, which leads to the decrease in k (the force constant) of the bond. Furthermore, the atomic weight of copper is greater than the atomic weight of silicon. Hence, the vibration frequencies (ν) decreased according to Equation (6), where c is the speed of light.

$$\nu = \left(\frac{1}{2\pi c}\right)\sqrt{\frac{k}{\mu}} \tag{6}$$

As illustrated in Figure 2(g), the peaks at 931.15 and 933.98 eV could be ascribed to the Cu $2p_{3/2}$ binding energies of Cu(I) and Cu(II) species. The peaks at 950.88 and

953.81 eV could be ascribed to the Cu $2p_{1/2}$ binding energies of Cu(I) and Cu(II) species (Xu *et al.* 2016). The two satellite peaks located at 941.85 and 961.54 eV were attributed to the +2 oxidation state (Hao *et al.* 2016). The XPS spectrum for Fe 2p region is shown in Figure 2(h); the peaks at 726.89 and 722.87 eV could be ascribed to the Fe $2p_{1/2}$ binding energies of Fe(III) and Fe(II) species, respectively. The peaks at 713.35 and 709.89 eV could be assigned to the Fe $2p_{3/2}$ binding energies of Fe(III) and Fe(II) species, respectively (Liu *et al.* 2016). Therefore, surface copper and iron of M2 exhibited complex valence (Cu^{2+}, Cu^{+}; Fe^{2+}, Fe^{3+}), the content of surface Cu^{2+} versus Cu^{+} was 2.51 and the content of surface Fe^{3+} versus Fe^{2+} was 1.1. The complex valence was beneficial to the redox cycle of Cu^{+}/Cu^{2+} and Fe^{2+}/Fe^{3+}, which could accelerate the formation of OH·.

Adsorption experiment

Before the degradation experiments, the adsorption amount of RhB on the surface of M2 was determined in absence of H_2O_2. M2, 1.0 g/L, was added into 250 mL dye solution. The solution was shaken at constant temperature and 2 mL was taken after a certain time interval to determine dye concentration. The relationship between adsorption amounts and time are shown in Figure 5(a). It can be seen that almost no differences in adsorption efficiency were observed after 25 min, indicating an adsorption–desorption equilibrium of the RhB within 25 min.

To study the adsorption mechanism of RhB onto M2, four adsorption kinetic models were used. The intraparticle diffusion model, pseudo-first-order kinetic model, pseudo-second-order kinetic model and Elovich model are described as Equations (7)–(10), respectively.

$$q_t = k_{id}t^{1/2} + C \tag{7}$$

$$q_t = q_e(1 - e^{-k_1 t}) \tag{8}$$

$$q_t = \frac{k_2 q_e^2 t}{1 + k_2 q_e t} \tag{9}$$

$$q_t = \frac{\ln(AB)}{B} + \frac{\ln(t)}{B} \tag{10}$$

where q_t (mg/L) is the amount of adsorbate adsorbed on the adsorbent at time t, k_{id} (mg/(g·min$^{0.5}$)) is the intraparticle diffusion rate constant, and C (mg/g) is a constant. q_e (mg/g) represents the quantity adsorbed at equilibrium, k_1 (min^{-1}) denotes the pseudo-first-order adsorption rate constant, and k_2 (g/(mg·min)) is the pseudo-second-order adsorption rate constant. A and B are experimental constants.

As shown in Figure 5(b), the experimental results fitted well with the pseudo-first-order kinetic model, pseudo-second-order kinetic model and Elovich model. The pseudo-second-order kinetic model was better correlated than the other two models. The parameters of each kinetic model are presented in Table S3.

The adsorption isotherm model of M2 was also studied and the results are shown in Figure 5(c). Langmuir and Freundlich isotherms are the most commonly used isotherms to describe the solid–liquid adsorption system. Freundlich and Langmuir isotherms are described as

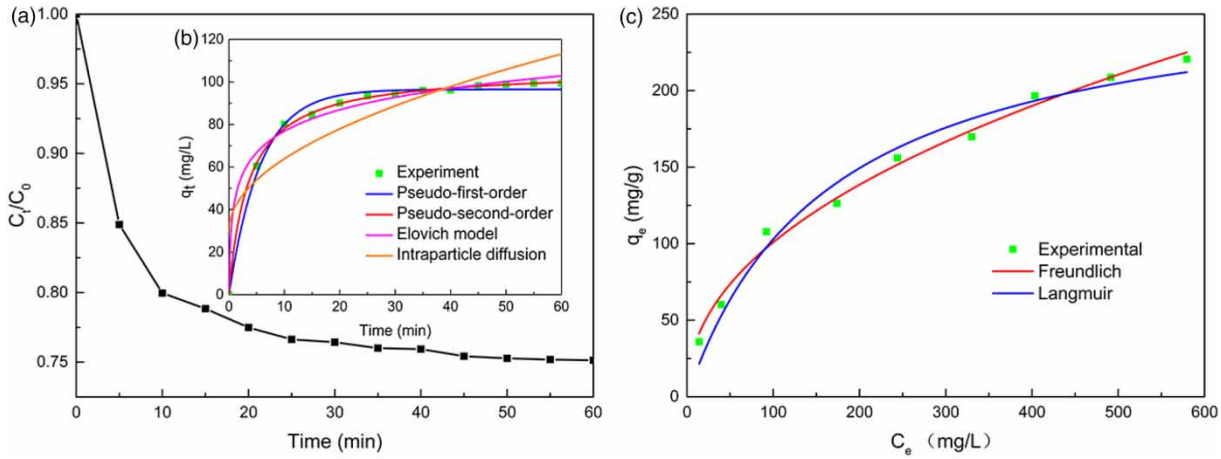

Figure 5 | Adsorption experiment of M2. (a) Adsorption properties of RhB (400 mg/L) over M2 (T = 60 °C). (b) The theoretical and experimental adsorption kinetic data of RhB (T = 60 °C). (c) The theoretical and experimental adsorption isotherm data of RhB (T = 20 °C). (Reaction conditions: catalyst dosage = 1.0 g/L, pH = 7.)

Equations (11) and (12), respectively.

$$\ln q_e = \ln K_f + \frac{1}{n} \times \ln C_e \tag{11}$$

$$\frac{C_e}{q_e} = \frac{1}{K_L q_m} + \frac{C_e}{q_m} \tag{12}$$

where q_e and C_e are the quantity of solute adsorbed at equilibrium (mg/g) and the equilibrium concentration of the adsorbate in aqueous solution (mg/L), respectively. q_m (mg/g) is the maximum monolayer adsorption capacity, K_L is the Langmuir adsorption constant (L/mg), which indicates the energy of adsorption. K_f is the Freundlich constant (mg/g), which indicates the adsorption extent, and n is the heterogeneity factor, which indicates the removal effectiveness.

As shown in Figure 5(c), the above two adsorption isotherm models fitted well with experimental results. The Freundlich isotherm was better correlated than Langmuir isotherm. The parameters of each adsorption isotherm model are shown in Table S4.

Evaluation of catalytic activity

Aiming to study the effects of different incorporated metal contents on dye degradation and to select the best catalyst, the degradation rate of different catalysts was compared under the same condition. The results are shown in Figure 6(a) and 6(b). It can be seen from Figure 6(a) that MCM-41 exhibited a quite low decolorization efficiency, only about 12.7% after 50 min. This was because MCM-41 lacked active metal copper and iron, resulting in the poor ability to produce hydroxyl radical. When aluminium was introduced, MCM-41-Al also performed badly with only 15.4% of decolorization efficiency after 50 min. This indicated that aluminium was not the active metal in this reaction. When iron was introduced, the catalytic ability of M0 enhanced a lot. Its decolorization efficiency reached about 54.9% after 50 min, but still very low. This was due to the high pH condition inhibiting the catalytic activity of iron. Comparing to M0, M1 containing copper performed much better. Its decolorization efficiency was 86.2% after 50 min. This can be explained by the synergistic effects of two-metal redox couples. Further increasing the amounts of introduced metals, the decolorization of M2 and M3 did not significantly increase (96.0% and 95.2% after 50 min, respectively). Comparing with M2 and M3, M0.5 contained more amounts of iron. However, its decolorization efficiency (84.9% after 50 min) was slightly lower than M2 and M3. This phenomenon was attributed to three reasons. Firstly, although the introduction of copper decreased the pH-dependence of the iron-based catalysts by synergistic effects, high pH condition severely inhibited the catalytic activity of iron. Secondly, copper exhibited higher catalytic activity by comparison with iron. Hence, M2 and M3 performed better. Thirdly, M0.5 possessed lower BET surface area by comparison with M2, which would influence the catalytic ability. The contents of Cu and Fe in M2-0 were the same as for M2 and M3. But M2-0 performed badly with only 76.0% of decolorization efficiency after 50 min. This was due to the small BET surface area of M2-0 resulting in few active sites. It was difficult to distinguish the catalytic ability between M2 and M3 because they exhibited similar decolorization efficiency. So we also measured COD removal of the solution and the results are shown in Figure 6(b). Both M2 and M3 had an excellent performance on the reduction of COD (43.2% and 42.3%, respectively). M2 exhibited a similar catalytic effect by comparison with M3 according to the results of decolorization efficiency and COD removal. But M2 had smaller amounts of copper than M3. To save the cost, M2 was chosen as the best catalyst to perform other experiments.

The variation trends of decolorization efficiency and COD removal are shown in Figure 6(c). The decolorization efficiency could reach 96.0% after 50 min, but the COD removal was only 43.2%. This was because OH· only partly degraded RhB into small molecule compounds. The utilization efficiency of H_2O_2 using COD removal as the index was 67.6%. To acquire higher COD removal, another 40 mM H_2O_2 was added after 50 min as shown in Figure 6(d). COD removal was further increased. The trend of H_2O_2 decomposition was consistent with COD removal and decolorization efficiency. Also, adding 40 mM H_2O_2 twice was better than adding 80 mM H_2O_2 once. So it was better to add intermittently.

The concentrations of leached copper ions and iron ions were measured by AAS. Repeated cycle experiments were also conducted to evaluate the stability of M2. M2 was reused three times, and each cycle lasted 50 minutes. After each cycle, the concentrations of leached copper ions and iron ions were tracked. The results are shown in Figure 6(e). During those three cycles, there was no notable reduction in decolorization efficiency and mineralization efficiency. The decolorization efficiency of the final test was 87.4% (8.6% less than the initial test). And the mineralization efficiency of the final test was 37.6% (5.6% less than the initial test cycle efficiency). The observed reduction of the degradation rate can be attributed to the decrease in the number of active

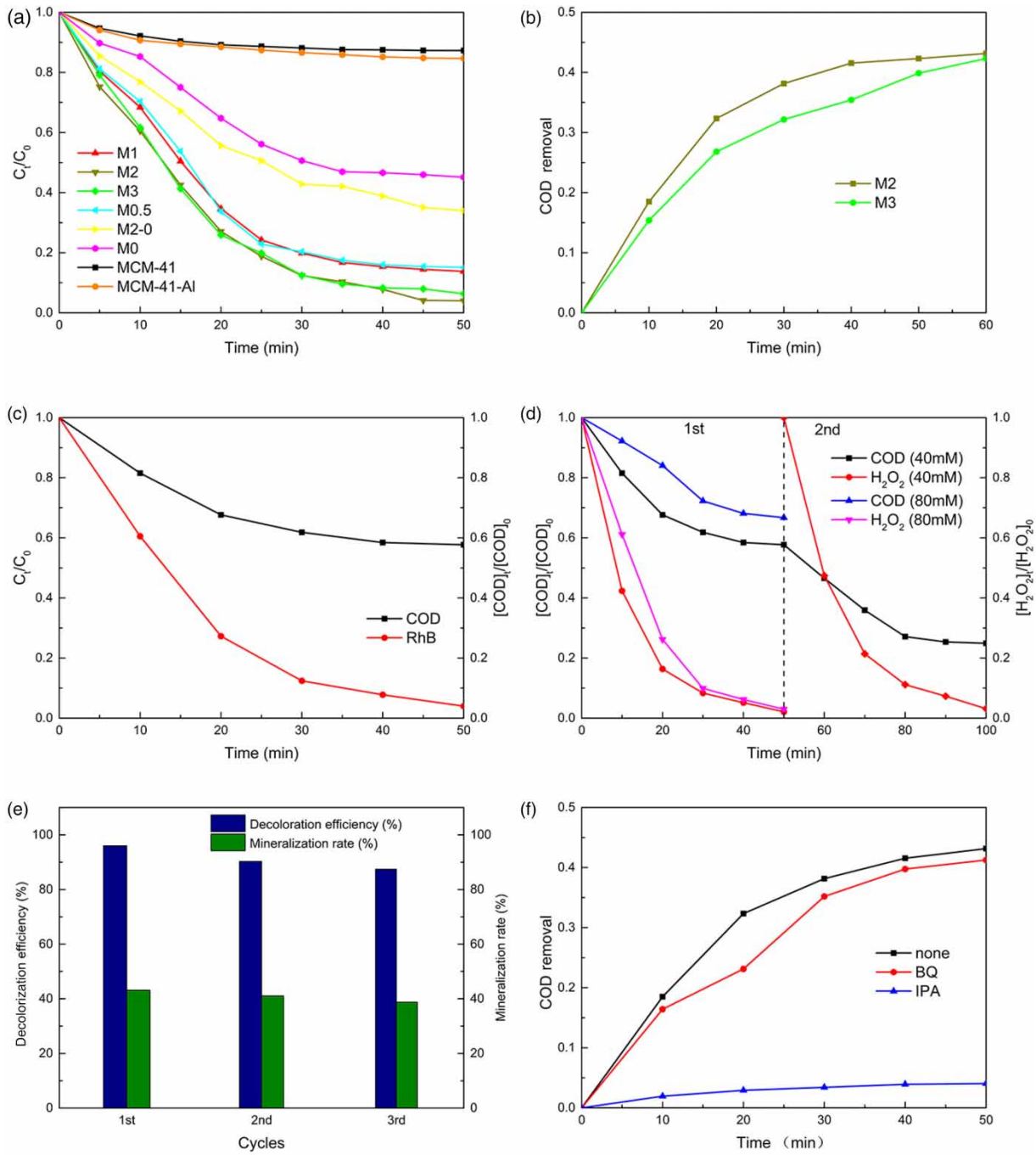

Figure 6 | Evaluation of the catalytic activity. (a) The decolorization efficiency of all samples. (b) The COD removal of M2 and M3. (c) The decolorization efficiency and COD removal of M2. (d) The consumption of H_2O_2 and the COD removal of M2. (e) The stability of M2 on the RhB degradation. (f) The effect of radical scavenger on the COD removal. (pH = 7, H_2O_2 dosage = 40 mM, initial dye concentration = 400 mg/L, temperature = 60 °C, catalyst dosage = 1 g/L.)

metal sites. The concentration of leached metal ions is shown in Table S5. After each cycle, the concentration of leached copper ions and iron ions decreased. This demonstrated that the stability of the reused catalysts was enhanced. The concentration of iron ions after each reaction was below the standard of the US Environmental Protection Agency (1.3 mg/L). So our material has favourable stability in RhB degradation.

To further investigate the radical species which contributes to RhB degradation, we used IPA and BQ to scavenge

OH· and O_2^-·, respectively. The concentration of the scavengers employed here was sufficient to inhibit OH· and O_2^-·. To avoid the influence made by intermediate products, we chose COD removal as the evaluation index. The results are shown in Figure 6(f). When IPA was added, COD removal remarkably decreased from 43.2 to 4.2%. Also, no obvious inhibitory effect was observed after adding BQ, implying that the contribution of O_2^-· to the degradation of RhB was negligible. The results indicated that OH· took the major role in RhB degradation.

The effect of different dyes on degradation rate was further examined. As shown in Figure S2, M2 was found to be effective on the degradation of RhB, MO, MB and CR. The decolorization efficiency of them was all larger than 85% within 50 min Hence, M2 has potential for wide application in dye wastewater treatment.

The reaction kinetics

To study the reaction kinetics, we did a series of experiments at different temperatures as shown in Figure 7(a). As expected, the decolorization efficiency was considerably increased with the increase of temperature. At 60 °C, the decolorization efficiency reached about 57.5 and 96.0% after 15 and 50 min, respectively. However, at 30 °C, the decolorization efficiency reached only about 59.2% after 50 min. This phenomenon could be attributed to three reasons. Firstly, a higher temperature could provide more energy for reactants to overcome the activation energy barrier. Secondly, the adsorption effect will be weak at a higher temperature and more reactive activity sites will be exposed which could accelerate the production of hydroxyl radical. Thirdly, increasing the temperature would enhance the viscosity and the surface tension of dye suspensions. Hence, the higher temperature would significantly enhance the mass transfer effect, increasing the collision frequency between hydroxyl radical and pollutant molecules.

The reaction kinetics of RhB degradation was simulated using the relative amounts, i.e. (C_t/C_0). The plots of [$\ln(C_t/C_0)$] versus t are presented in Figure 7(b). The plots yielded straight lines; therefore the kinetics of RhB degradation was found to be first-order. The results were consistent with the literature. The equation of first-order kinetics was described as Equation (13)

$$\ln\frac{C_t}{C_0} = -kt \tag{13}$$

where k is the apparent first-order rate constant (min^{-1}), t is the reaction time (min), C_0 is the initial concentration of RhB and C_t is the concentration of RhB at time t. The value of k was 0.0660 min^{-1} ($R^2 = 0.997$), 0.0445 min^{-1} ($R^2 = 0.997$), 0.0322 min^{-1} ($R^2 = 0.998$) and 0.0203 min^{-1} ($R^2 = 0.989$) at 60, 50, 40 and 30 °C, respectively. According to the Arrhenius equation described as Equation (14), the value of E_a could be obtained by calculating the slope of ln k versus $1/T$ (Figure 7(c)). The value of E_a was 32.4 kJ/mol.

$$\ln k = \ln A - \frac{E_a}{RT} \tag{14}$$

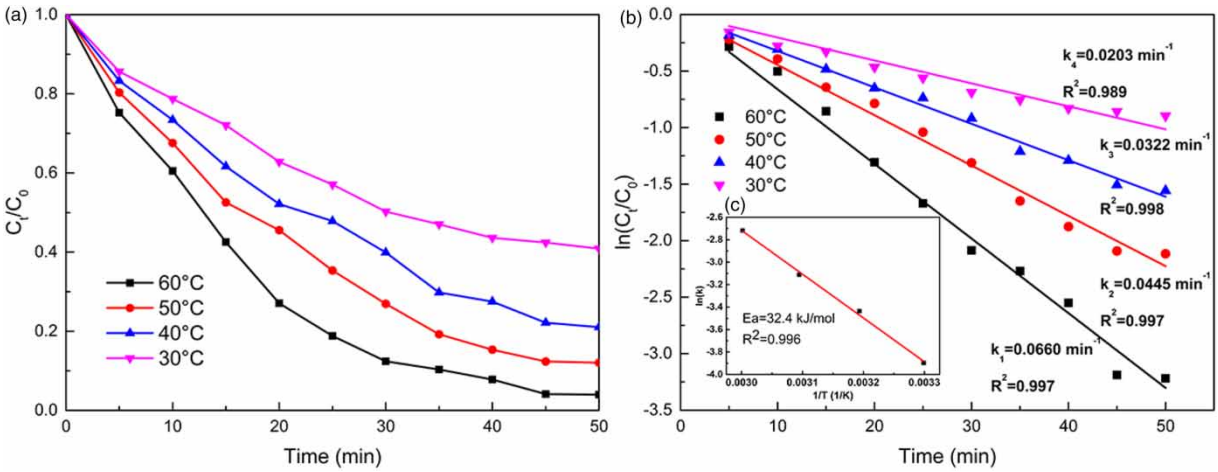

Figure 7 | The effect of temperature on the RhB degradation and the kinetics data of the reaction. (a) The decolorization efficiency of RhB at different temperatures. (b) Plots of $\ln(C_t/C_0)$ versus time for the RhB degradation. (c) Plots of ln(k) versus ($1/T$). (pH = 7, initial dye concentration = 400 mg/L, H_2O_2 dosage = 40 mM, M2 dosage = 1 g/L.)

where R is the universal gas constant (8.314 J/(mol·K)), A is a constant, k is the rate constant, E_a is the activation energy and T is temperature.

Effect of the reaction conditions

The effect of H_2O_2 dosage on RhB degradation was investigated at 10, 20, 30, 40, 50 and 80 mM. The results are shown in Figure 8(a). The dosage of H_2O_2 was directly related to the amounts of hydroxyl radicals generated in the Fenton reaction. Hence, the dosage of H_2O_2 significantly influenced the initial reaction rate. It could be noticed that when the dosage of H_2O_2 increased from 10 to 40 mM, the decolorization efficiency increased from 37.6 to 89.7% after 35 min. This phenomenon could be explained by the high initial concentration of H_2O_2 that could produce more hydroxyl radicals which possessed greater degradation ability. However, further increasing the dosage of H_2O_2 did not enhance the decolorization efficiency. In the beginning, 50 mM of H_2O_2 exhibited a better decolorization efficiency (29.0%) than 40 mM of H_2O_2 (24.8%) after 5 min. However, its final decolorization efficiency (75.9%) was far below the 40 mM of H_2O_2 (96.0%) after 50 min. When 80 mM of H_2O_2 was added, the decolorization efficiency was lower than the 40 mM of H_2O_2. This phenomenon was because higher dosage of H_2O_2 could produce more hydroxyl radicals at the beginning, which increased the catalytic efficiency. However, the excessive H_2O_2 would react with hydroxyl radicals (Equations (15) and (16)), resulting in a decrease in the

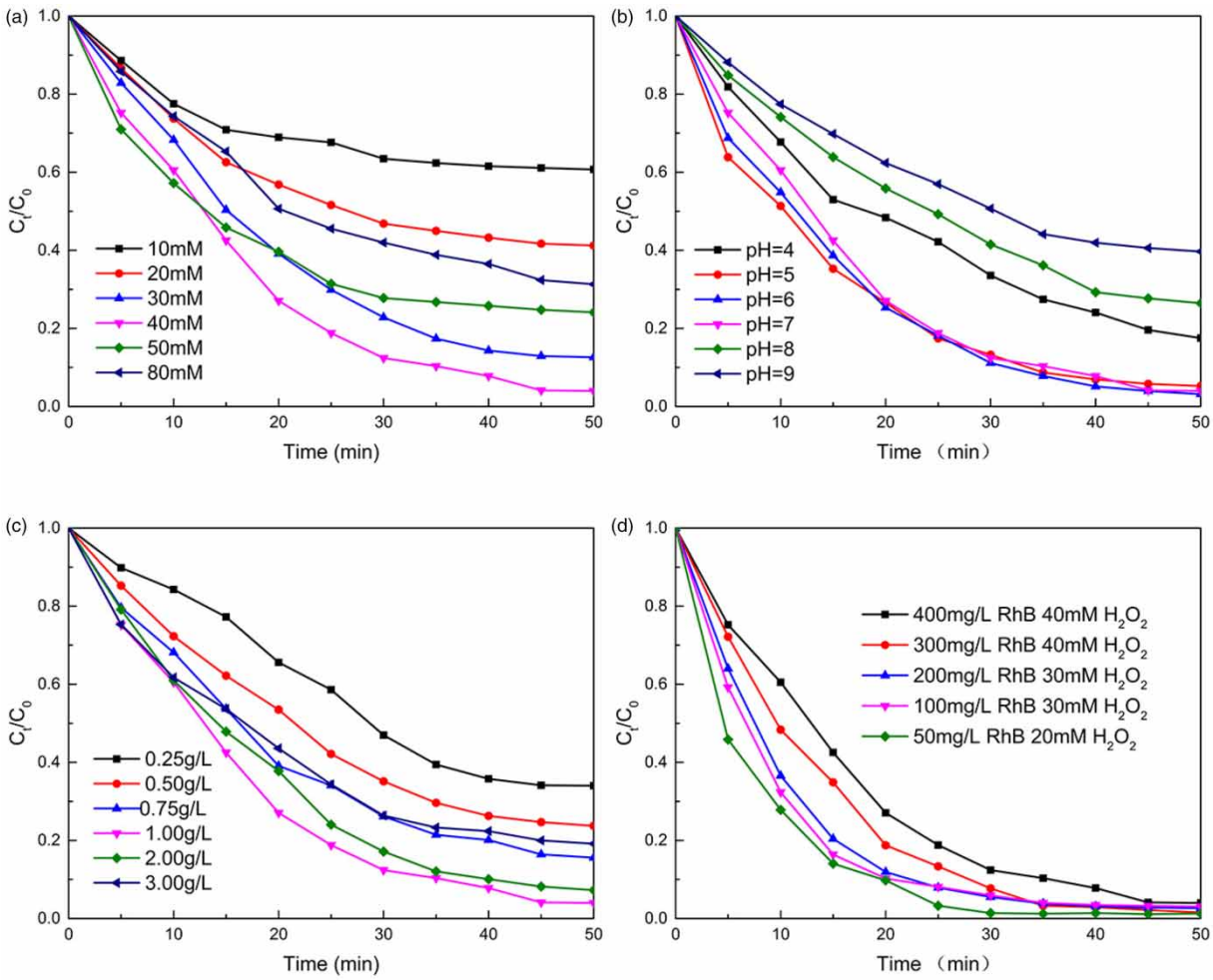

Figure 8 | The effect of the reaction conditions on the RhB degradation. (a) The effect of H_2O_2 dosage on the RhB degradation. (b) The effect of pH on the RhB degradation. (c) The effect of catalyst dosage on the RhB degradation. (d) The effect of dye concentration on the RhB degradation. (Reaction conditions: T = 60 °C, pH = 7, initial dye concentration = 400 mg/L, H_2O_2 dosage = 40 mM and M2 dosage = 1 g/L.)

total amounts of hydroxyl radicals in the solution. Hence, 40 mM of H_2O_2 was chosen as the optimal dosage of H_2O_2.

$$H_2O_2 + OH\cdot \rightarrow HO_2\cdot + H_2O \quad (15)$$

$$HO_2\cdot + OH\cdot \rightarrow H_2O + O_2 \quad (16)$$

The effect of initial pH on the RhB degradation was investigated from 4 to 9 by adding a moderate dosage of NaOH or HCl. The results are shown in Figure 8(b). It is well-known that homogeneous classical Fenton reaction performs well only in a narrow pH range (2–4). And some iron-containing heterogeneous catalysts also perform badly when the pH is greater than 5. However, our catalyst exhibited good performance in a wider pH range. The optimum decolorization efficiency was 95.3% after 35 min when the pH is near neutral. When the pH increased from 4 to 7, the decolorization efficiency after 50 min increased from 82.5 to 96.0%. M2 also had an excellent decolorization efficiency (96.8%) when the pH is 6. Further increasing the pH did not enhance the catalytic effect. When pH is 8 and 9, the decolorization efficiency was only 73.5 and 60.3% after 50 min, respectively. This phenomenon was because the co-operation of copper and iron could improve the reactivity of iron because of the high standard reduction potential difference (0.78 V) between Cu and Fe. Hence, the limitation of pH was broken. Furthermore, hydroxyl radicals could react with OH^- to generate $HO_2\cdot$, and $HO_2\cdot$ had lower reactivity. Also, H_2O_2 decomposed into H_2O and O_2 easily at higher pH (Equations (17) and (18)). The neutral pH was chosen as the optimal initial pH because of the high decolorization efficiency and no need for the subsequent neutralized disposition of pH after treatment.

$$OH\cdot + 2OH^- \rightarrow HO_2\cdot + H_2 \quad (17)$$

$$2H_2O_2 \rightarrow O_2 + 2H_2O \quad (18)$$

The appropriate dosage of catalysts could enhance the catalytic ability and the excessive dosage of catalysts is wasteful and costly. Hence, the effect of the dosage of catalysts on the RhB degradation was evaluated using 0.25, 0.50, 0.75, 1.0, 2.0 and 3.0 g/L of catalysts, respectively. The results are shown in Figure 8(c). When the dosage of catalysts increased from 0.25 to 1 g/L, the decolorization efficiency increased a lot. The decolorization efficiency after 50 min reached 66.0, 76.3, 84.4 and 96.0% when the dosage of catalysts was 0.25, 0.50, 0.75 and 1.0 g/L, respectively. This was because higher dosage of catalysts possessed more active metal sites which could produce more free-radical species to promote RhB degradation. However, further increasing the dosage of catalysts did not promote RhB degradation. When the dosage of catalysts was 2.0 and 3.0 g/L, the decolorization efficiency after 50 min reached 92.7 and 80.9%, respectively. This phenomenon could be explained by two reasons. On the one hand, increasing the dosage of catalysts could accelerate the generation of hydroxyl radicals. Hydroxyl radicals would react with H_2O_2, which leads to fewer hydroxyl radicals in the solution by comparison with 1.0 g/L of catalysts. On the other hand, hydroxyl radicals might be scavenged by excessive metal species of superfluous catalysts (Equation (19)). Based on the above results, 1.0 g/L of catalysts was chosen as the optimal dosage in RhB degradation.

$$Cu^+ + OH\cdot \rightarrow Cu^{2+} + OH^- \quad (19)$$

The effect of the different initial concentration of RhB (50–400 mg/L) on degradation reaction was also studied and the results are shown in Figure 8(d). To prevent the excessive dosage of H_2O_2 influencing the final degradation efficiency, lower dosage of H_2O_2 was added into the low concentration of RhB solution. The initial decolorization efficiency decreased when increasing the initial concentration of dyes. After 5 min, the decolorization efficiency of 50, 100, 200, 300 and 400 mg/L of RhB was 54.1, 40.8, 36.0, 27.8 and 24.8%, respectively. But the total amounts of dye degraded increased. Greater amounts of dye molecules would adsorb on the catalysts' surface when increasing the initial concentration of dyes. Large amounts of dye molecules adsorbed on the catalysts' surface decreased the number of active metal sites, which limited the production of hydroxyl radicals. However, the higher concentration of dyes increased the collision frequency of molecules, which accelerated the reaction rate. After 50 min, the decolorization efficiency of 50, 100, 200, 300 and 400 mg/L of RhB reached 98.7, 96.9, 97.3, 98.5 and 96.0%, respectively. Hence, our catalyst could degrade not only the low concentration of dyes but also the high concentration of dyes, which suggests the catalyst has a bright prospect in dye wastewater treatment.

CONCLUSIONS

In summary, a series of Cu- and Fe-doped Al-MCM-41 heterogeneous Fenton catalysts with different contents of metal were synthesized by the co-precipitation method.

Among them, M2 exhibited the best catalytic activity on 400 mg/L RhB degradation, and could achieve 96.0% decolorization efficiency and 43.2% COD removal using only 40 mM H_2O_2 within 50 min. Further adding H_2O_2 would increase the mineralization rate. M2 also showed excellent stability and could be reused at least three times without any obvious deterioration in catalytic activity. Fenton reaction had a significant acceleration effect and was less pH-dependent when Cu was introduced. But the excessive amounts of Cu would break MCM-41's structure. Al had nearly no effect on RhB degradation but could sustain MCM-41's structure. Free radical capture experiments demonstrated that OH· was the main reactive species. M2 exhibited excellent catalytic activity in a wide pH range, had high stability, required smaller dosage of reactants and had high utilization efficiency of H_2O_2, demonstrating a promising future in wastewater treatment.

DATA AVAILABILITY STATEMENT

All relevant data are included in the paper or its Supplementary Information.

REFERENCES

Alonso Lemus, I. L., Verde-Gómez, Y. & Alvarez Contreras, L. 2010 Platinum nanoparticles synthesis supported in mesoporous silica and its effect in MCM-41 lattice. *International Journal of Electrochemical Science* **6** (9), 4176–4187.

Bokare, A. D. & Choi, W. 2014 Review of iron-free Fenton-like systems for activating H_2O_2 in advanced oxidation processes. *Journal of Hazardous Materials* **275**, 121–135.

Corrêa, M. L. S., Wallau, M. & Schuchardt, U. 1997 Synthesis and characterization of chromo, ferro, mangano and vandio silicates with MTW structure. *Studies in Surface Science and Catalysis* **105**, 277–284.

Dai, C., Tian, X., Nie, Y., Lin, H.-M., Yang, C., Han, B. & Wang, Y. 2018 Surface facet of $CuFeO_2$ nanocatalyst: a key parameter for H_2O_2 activation in Fenton-like reaction and organic pollutant degradation. *Environmental Science & Technology* **52** (11), 6518–6525.

Eberhardt, M. K., Ramirez, G. & Ayala, E. 1989 Does the reaction of copper(I) with hydrogen peroxide give hydroxyl radicals? A study of aromatic hydroxylation. *The Journal of Organic Chemistry* **54** (25), 5922–5926.

El-Sharkaway, E. A., Kamel, R. M., El-Sherbiny, I. M. & Gharib, S. S. 2020 Removal of methylene blue from aqueous solutions using polyaniline/graphene oxide or polyaniline/reduced graphene oxide composites. *Environmental Technology* **41** (22), 2854–2862.

Hao, J., Yang, W., Huang, Z. & Zhang, C. 2016 Superhydrophilic and superaerophobic copper phosphide microsheets for efficient electrocatalytic hydrogen and oxygen evolution. *Advanced Materials Interfaces* **3** (16), 1600236.

Kong, Y., Zhu, H. Y., Yang, G., Guo, X. F., Hou, W. H., Yan, Q. J., Gu, M. & Hu, C. 2004 Investigation of the structure of MCM-41 samples with a high copper content. *Advanced Functional Materials* **14** (8), 816–820.

Kumar, K.-N. P., Kumar, J. & Keizer, K. 1994 Effect of peptization on densification and phase-transformation behavior of sol–gel-derived nanostructured titania. *Journal of the American Ceramic Society* **77** (5), 1396–1400.

Lin, H.-P., Wong, S.-T., Mou, C.-Y. & Tang, C.-Y. 2000 Extensive void defects in mesoporous aluminosilicate MCM-41. *The Journal of Physical Chemistry B* **104** (38), 8967–8975.

Ling, Y., Long, M., Hu, P., Chen, Y. & Huang, J. 2014 Magnetically separable core–shell structural γ-Fe_2O_3@Cu/Al-MCM-41 nanocomposite and its performance in heterogeneous Fenton catalysis. *Journal of Hazardous Materials* **264**, 195–202.

Liu, B. S., Xu, D. F., Chu, J. X., Liu, W. & Au, C. T. 2007 Deep desulfurization by the adsorption process of fluidized catalytic cracking (FCC) diesel over mesoporous Al-MCM-41 materials. *Energy & Fuels* **21** (1), 250–255.

Liu, J., Zheng, M., Shi, X., Zeng, H. & Xia, H. 2016 Amorphous FeOOH quantum dots assembled mesoporous film anchored on graphene nanosheets with superior electrochemical performance for supercapacitors. *Advanced Functional Materials* **26** (6), 919–930.

Lu, M.-C., Chen, J.-N. & Chang, C.-P. 1999 Oxidation of dichlorvos with hydrogen peroxide using ferrous ion as catalyst. *Journal of Hazardous Materials* **65** (3), 277–288.

Ma, X., Cheng, Y., Ge, Y., Wu, H., Li, Q., Gao, N. & Deng, J. 2018 Ultrasound-enhanced nanosized zero-valent copper activation of hydrogen peroxide for the degradation of norfloxacin. *Ultrasonics Sonochemistry* **40**, 763–772.

Nogueira, R. F. P., Oliveira, M. C. & Paterlini, W. C. 2005 Simple and fast spectrophotometric determination of H_2O_2 in photo-Fenton reactions using metavanadate. *Talanta* **66** (1), 86–91.

Parida, K. M. & Rath, D. 2007 Structural properties and catalytic oxidation of benzene to phenol over CuO-impregnated mesoporous silica. *Applied Catalysis A: General* **321** (2), 101–108.

Parida, K. M. & Rath, D. 2009 Surface characterization and catalytic evaluation of copper-promoted Al-MCM-41 toward hydroxylation of phenol. *Journal of Colloid and Interface Science* **340** (2), 209–217.

Roonasi, P. & Nezhad, A. Y. 2016 A comparative study of a series of ferrite nanoparticles as heterogeneous catalysts for phenol removal at neutral pH. *Materials Chemistry and Physics* **172**, 143–149.

Sing, K. S. W., Everett, D. H., Haul, R. A. W., Moscou, L., Pierotti, R. A., Rouquérol, J. & Siemieniewska, T. 1985 Reporting physisorption data for gas/solid systems with special reference to the determination of surface area and porosity (Recommendations 1984). *Pure and Applied Chemistry* **57** (4), 603–619.

Sobczak, I., Ziolek, M., Renn, M., Decyk, P., Nowak, I., Daturi, M. & Lavalley, J.-C. 2004 Cu state and behaviour in MCM-41 mesoporous molecular sieves modified with copper during the synthesis—comparison with copper exchanged materials. *Microporous and Mesoporous Materials* **74** (1), 23–36.

Srinivas, N., Radha Rani, V., Kulkarni, S. J. & Raghavan, K. V. 2002 Liquid phase oxidation of anthracene and trans-stilbene over modified mesoporous (MCM-41) molecular sieves. *Journal of Molecular Catalysis A: Chemical* **179** (1), 221–231.

Xia, M., Chen, C., Long, M., Chen, C., Cai, W. & Zhou, B. 2011a Magnetically separable mesoporous silica nanocomposite and its application in Fenton catalysis. *Microporous and Mesoporous Materials* **145** (1), 217–223.

Xia, M., Long, M., Yang, Y., Chen, C., Cai, W. & Zhou, B. 2011b A highly active bimetallic oxides catalyst supported on Al-containing MCM-41 for Fenton oxidation of phenol solution. *Applied Catalysis B: Environmental* **110**, 118–125.

Xu, J., Li, Y., Yuan, B., Shen, C., Fu, M., Cui, H. & Sun, W. 2016 Large scale preparation of Cu-doped α-FeOOH nanoflowers and their photo-Fenton-like catalytic degradation of diclofenac sodium. *Chemical Engineering Journal* **291**, 174–183.

First received 22 December 2020; accepted in revised form 22 February 2021. Available online 4 March 2021